Reconfigurable plug-and-play assembly for the continuous production of composite anodes for modulating lithium storage

Jiseok Lim[a], Jungho Hwang[b,*], Jeong Hoon Byeon[a,*]

[a] School of Mechanical Engineering, Yeungnam University, Gyeongsan 38541, Republic of Korea
[b] School of Mechanical Engineering, Yonsei University, Seoul 03722, Republic of Korea

HIGHLIGHTS

- A plug-and-play assembly platform yielded lithium anodes with modulatable capacity.
- The platform can be extended for on-demand manufacture of different lithium anodes.
- The different architectures enabled the modulation of lithium storage performance.

GRAPHICAL ABSTRACT

Modulating lithium storage was achieved by developing a single-pass plug-and-play assembly platform for the built-to-order manufacture of different composite anodes comprising a transition metal oxide, a carbon matrix, and a conductive polymer.

ARTICLE INFO

ABSTRACT
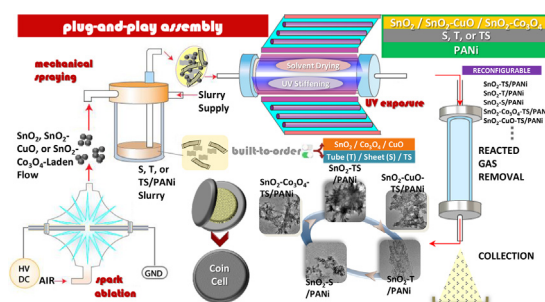
In this study, modulating lithium storage is achieved as a result of the built-to-order assembly of composite anodes by the serial connection of reconfigurable plug-and-play devices in an ambient atmosphere. In this assembly, spark ablation, mechanical spraying, and ultraviolet exposure devices are connected in series, as well as the turning of devices, under a continuous air flow, affording composite anodes in less than 15 s. Specifically, SnO_2 nanoparticles prepared from spark ablation are carried by air flow, and the flow is injected into a mechanical spray system to generate carbon nanotube–graphene nanosheet/polyaniline slurry droplets, where SnO_2 nanoparticles are inserted into the droplets via gas pressurization at the spray nozzle. Subsequently, the droplets are passed through a 254-nm ultraviolet lamp and a silica–gel–installed hollow tube for dynamic stiffening and drying to form SnO_2-carbon nanotube–graphene nanosheet/polyaniline composites in a single-pass air flow. In addition, different composites such as SnO_2-carbon nanotube (or graphene nanosheet)/polyaniline, SnO_2—CuO-carbon nanotube–graphene nanosheet/polyaniline, and SnO_2—Co_3O_4-carbon nanotube–graphene nanosheet/polyaniline are conveniently assembled by the reconfiguration of metal oxide nanoparticles or carbon/polymer slurries in the plug-and-play operation. These composites are suitable as anodes for lithium storage and enabled the modulation of specific capacities, rate capabilities, and cyclabilities by employing different architectures.

1. Introduction

Over the past decade, lithium-based batteries have been extensively investigated for their use in electric vehicles and various electronic devices [1]. To achieve high energy density and cycle stability, as well as light-weight nature and cost-effectiveness, in particular, the development of optimal active materials and architectures for lithium anodes has been considered as one of the most critical factors for practical applications [2]. Even though previous studies have reported important parameters, such as lithium (sodium, potassium, or magnesium)–ion, lithium–sulfur, lithium–air, and lithium–metal configurations, for providing commercial opportunities to energy-storage devices [3], the assembly approaches for anodes introduced previously have been based on batch-wise harsh chemistries, which do not satisfy several criteria for realization, including environmental friendliness [1,4]. More recently, the optimization of the assembly process of anode materials also has been strongly recommended to reduce greenhouse gas emissions from the manufacturing of lithium batteries [5]. Hence, it is desirable to explore versatile platforms for the efficient assembly of anode materials with desirable performance and durabilities with low waste generation, as well as helping stakeholders of the battery industry [6,7].

The practical applications of newly developed anode materials are directly related not only to the optimal selection of compositions and architectures but also to the innovative production technologies. To achieve the successful translation of promising anode materials from the bench top, spraying (i.e., aerosol)-enabled anode assemblies have recently become attractive for the continuous production and customization of anode materials [8]. Spray pyrolysis approaches have been frequently employed as a continuous production platform to construct perforated or holey microstructures for highly reversible lithium-storage capacities [9–11]. In addition, spraying has been used for the classification of suitable precursor–solvent combinations for the cost-effective manufacturing of anode materials [12]. Nevertheless, spraying not only requires templates and toxic chemicals to form porous structures but also high-temperature atmospheres to induce the pyrolysis of precursors, indicating that the achievement of an environmentally benign, versatile assembly platform for manufacturing anode materials is challenging. Moreover, the introduction of digitizable devices for automating anode assemblies has been raised recently [7], in which the assembly platform comprises digitally operable devices to conveniently respond to various assembly requirements although relevant studies on digitizable anode assemblies have not been reported.

In this study, a plug-and-play platform is developed for the built-to-order manufacturing of composite anodes by connecting spark ablation; mechanical spraying; and ultraviolet (UV) exposure devices in series (Fig. 1A). This requires only pushing the power button of the devices to yield composite anodes in a single-pass, continuous configuration. These three devices can be electrically controlled to continuously generate transition metal oxide (TMO: SnO_2, SnO_2−CuO, and SnO_2−Co_3O_4) nanoparticles (NPs); carbon (carbon nanotubes [T] and/or graphene nanosheets [S])/polymer (polyaniline; PANi) slurry droplets; and stiffened-dried composites (SnO_2-TS/PANi, SnO_2–CuO-TS/PANi, and SnO_2−Co_3O_4-TS/PANi, including SnO_2-T/PANi and SnO_2-S/PANi; Fig. S1) under an ambient single-pass air flow. Specifically, atmospheric pressure spark ablation between two TM rods produced metal vapors under room-temperature air flow, and the vapors converted into TMO particles of a few nanometers via nucleation–condensation. This nanodimension is suitable to overcome the volume change or aggregation of the TMO particles during charge–discharge [13]. The TMO-NP-laden air flow was directly used as an operating fluid, generating droplets of TS (or T or S)/PANi in a dimethyl sulfoxide (DMSO; Sigma-Aldrich) slurry. During mechanical spraying, the air-suspended TMO NPs were included in the droplets via gas pressurization near the spray nozzle to form hybrid droplets. Subsequently, the droplets were dynamically stiffened and dried by passing through a 254-nm UV lamp and the silica-gel-installed hollow tube, leading to the formation of composites in an assembly time of less than 15 s. The TMO-carbon/polymer architecture was selected to demonstrate a reconfigurable assembly for achieving modulating lithium storage capacities with high performance because the architecture was verified to prevent unwanted aggregation or volume change of TMO NPs and accelerate charge transfer between TMO NPs via the conductive paths of carbon/polymer matrices [9,14–18]. Currently, scalable syntheses of T and S in commercial quantities for numerous industrial applications have been reported [19–22]; furthermore, the carbon/PANi structure exhibits improved stability during electrochemical cycling [16,23–25], implying that utilizing an architecture is suitable to provide practical opportunities for the built-to-order manufacture of anodes. The resulting composites ($1.25 \, g \, cm^{-3}$ packing density and $2.05 \, mg \, cm^{-2}$ areal composite mass loading) were employed as anode materials to determine lithium-storage capacity and cycle stability performance. In addition, the physicochemical characteristics of the assembled composites were investigated to confirm the reconfigurable assembly of the plug-and-play platform.
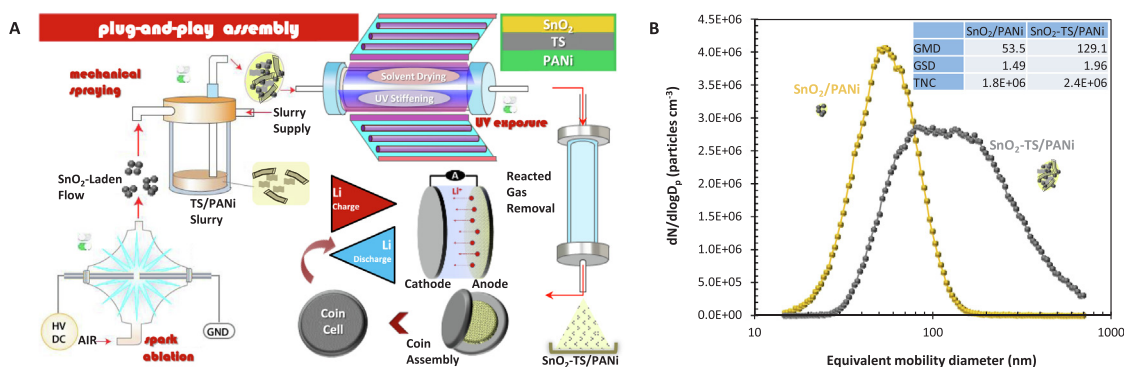

Fig. 1. (A) Gas-phase single-pass assembly for composite lithium anodes (SnO_2-TS/PANi) with digitizable systems, spark ablation, mechanical spraying, and UV exposure connected in series. Spark ablation between two identical Sn rods yields SnO_2 NPs from the atmospheric-pressure plasmas under an air flow. A TS/PANi (in DMSO) slurry is constantly supplied into the mechanical spraying device, while the SnO_2 NP-laden air flow is used as an operating fluid in the mechanical spraying device to generate mixed droplets of SnO_2, TS, and PANi. These droplets are directly passed through a 254-nm UV lamp and silica-gel-installed hollow tube for the dynamic stiffening and drying of droplets, yielding SnO_2-TS/PANi composites. Next, the composites are dispensed to fabricate lithium anodes for electrochemical analyses. (B) Size distributions of assembled SnO_2/PANi and SnO_2-TS/PANi composites using an SMPS. Summaries of the distributions are shown in the inset table, and GMD, GSD, and TNC values for SnO_2/PANi increase with the TS incorporation (depicted inset graphics of SnO_2/PANi and SnO_2-TS/PANi).
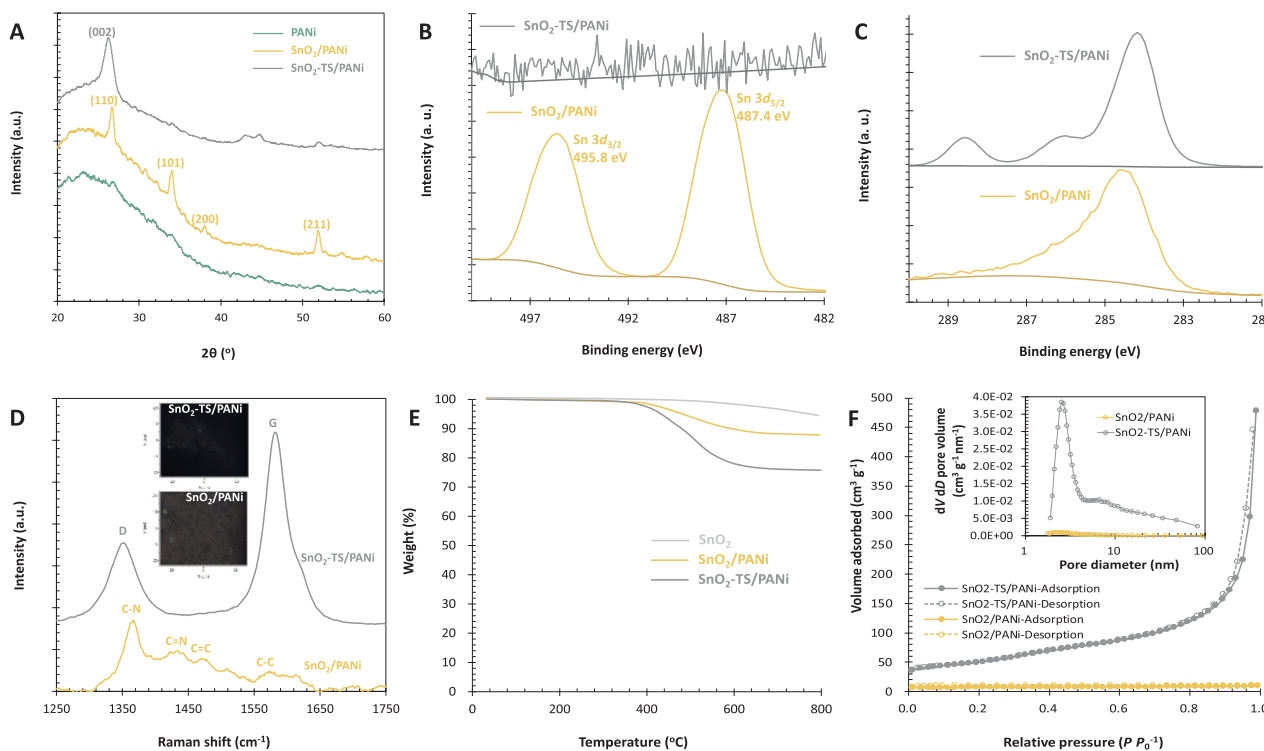
Fig. 2. Characterization of the assembled SnO_2/PANi and SnO_2-TS/PANi composites. (A) XRD patterns of the composites, including individual PANi particles. (B, C) Sn 3*d* and C 1*s* core-level XPS spectra of the composites. (D) Raman spectra of the composites with optical images of the scanned regions of the specimens (insets). (E) TGA results of the composites, including individual SnO_2 NPs. (F) Adsorption–desorption isotherms of the composites. Inset shows the pore size distributions of the composites.

2. Results and discussion

First, the size distributions of SnO_2/PANi and SnO_2-TS/PANi were estimated using a scanning mobility particle sizer (SMPS; 3936, TSI, USA) via the investigation of the aerosol formed by the merging of SnO_2 (from spark ablation) and TS/PANi for the assembly of SnO_2-TS/PANi. The incorporation of PANi and TS/PANi with SnO_2 NPs did not induce a bi- or multi-modal distribution (i.e., exhibited a uni-modal distribution for both cases, Fig. 1B), indicating that merging SnO_2 and PANi (or TS/PANi) is sufficiently robust even in a single-pass assembly to construct composite structures (inset diagrams of Fig. 1B) during spraying and subsequent UV exposure. The increase in the geometric mean diameter (GMD) was rather significant compared with those of the geometric standard deviation (GSD) and total number concentration (TNC) because of the additional incorporation of S (inset table of Fig. 1B). In addition, the mass fractions of SnO_2, TS, and PANi components were monitored using a piezobalance particle monitor (3522, Kanomax, Japan), which were 0.38, 0.48, and 0.14, respectively.

X-ray diffraction (XRD; D/MAX-2500, Rigaku, Japan) profiles revealed peaks characteristic of SnO_2/PANi and SnO_2-TS/PANi, including those of individual PANi (Fig. 2A). A broad band observed at ~25° (2θ) for PANi correspond to the presence of PANi crystallites, and the band intensity decreased by the incorporation of SnO_2 or SnO_2-TS. Peaks characteristic of tetragonal SnO_2 with a cassiterite structure (JSPDS Card No. 41-1445) were observed for SnO_2/PANi [26], demonstrating that spark ablation under an air flow is suitable to produce crystalline SnO_2 NPs. The average crystallite size estimated by the Scherrer equation was 3.9 nm; this size is similar to the effective nanoscale level to prevent a significant volume change during charge–discharge [13]. Interestingly, these characteristic SnO_2 peaks were significantly weakened, as well as the (1 1 0) band corresponding to TS was not observed, with the further incorporation of TS, possibly related to the mutual interference between SnO_2 and TS during measurement [27],

including another interference from coexisting PANi; thus, a low degree of SnO_2 crystallinity and TS graphitization is simultaneously observed. This result further supported strong incorporation among the components during the single-pass assembly without the significant dislocation of SnO_2, TS, or PANi. X-ray photoelectron spectroscopy (XPS; Axis-HIS, Kratos Analytical, Japan) profiles also matched the changes in the characteristic SnO_2 spectrum by the incorporation of TS/PANi (Fig. 2B and C). Even though characteristic bands for carbon-containing groups (C—C [284.8 eV], C—O [286.2 eV], and O—C=O [288.6 eV]) were clearly observed by incorporation [28], the core-level bands for SnO_2 (with binding energies of 495.6 and 487.2 eV, respectively, corresponding to Sn $3d_{3/2}$ and $3d_{5/2}$) were dissipated significantly [29]. Much smaller primary sizes of SnO_2 particles than those of T and S might induce attenuation of Sn signals during the measurement. Fourier-transform infrared (FTIR; Nicolet iS 10, Thermo Fisher Scientific, USA) spectrum of SnO_2-TS/PANi exhibits oxygen containing groups (—OH and C=O) [30], including the bending vibration of N–H (Fig. S2) [31]. This result also implied that a majority of the SnO_2 NPs are possibly present within the TS matrices and are subsequently covered by PANi during the assembly due to capillary suction from the voids of TS matrices [32]. In addition, analogous phenomena were observed for SnO_2-T/PANi and SnO_2-S/PANi (Fig. S3A and B), implying that the proposed assembly can be reconfigured to achieve similar architectures even with different carbon matrices. The dominant carbonaceous surfaces of the assembled SnO_2-T/PANi and SnO_2-S/PANi (aerosol directly deposited on glass discs, inset images) were further verified by Raman spectroscopy (XploRA Plus, Horiba, Japan; Fig. 2D). The bands observed at ~1360 cm^{-1} and 1430 cm^{-1} corresponded to the C–N stretching and C=N stretching vibrations of the imines in SnO_2/PANi, respectively, while two typical graphitic carbon peaks at ~1330 cm^{-1} (*D* band) and ~1580 cm^{-1} (*G* band) were predominantly observed for SnO_2-TS/PANi, respectively (analogous results were observed for SnO_2-T/PANi and SnO_2-S/PANi, as shown in Fig. S3C),

representing the main surface compositions of the specimens. Thermogravimetric analysis (TGA; Diamond TG/DTA, Perkin Elmer, USA) of SnO_2/PANi and SnO_2-TS/PANi, including SnO_2 NPs, performed under nitrogen (20–800 °C) revealed thermally decomposed or degraded fractions (Fig. 2E). SnO_2-TS/PANi (prepared from the trial-and-error approach with modulating concentration of TS/PANi for the mechanical spraying to minimize segregation of SnO_2 and TS/PANi components from the composite) exhibited a weight loss of 26.2%, predominantly related to the gasfication of the pyrolyzable components of TS/PANi. The TGA curve of SnO_2/PANi showed a loss of 16.4%, which was comparable to the mass fraction of PANi in SnO_2-TS/PANi measured using a piezobalance particle monitor. Significant weight losses were not observed after high-temperature treatment, possibly related to the feasibility of dynamic UV stiffening and drying processes to form thermally stable structures. The adsorbed volume and pore size distribution of SnO_2-TS/PANi analyzed using a porosimeter (ASAP 2010, Micromeritics, USA) were remarkably improved in comparison to SnO_2/PANi ($21.7\,m^2\,g^{-1}$ specific surface area [SSA]) by the further incorporation of TS (Fig. 2F), implying that the incorporation of TS possibly facilitates the formation of porous matrices, which compensate for the volume expansion and enhance the transport of charges during electrochemical cycling [33]. In addition, improved textures were observed for SnO_2-T/PANi and SnO_2-S/PANi (Fig. S3D), verifying the reconfiguration capability of the plug-and-play platform. The adsorption isotherm for SnO_2-TS/PANi ($225.7\,m^2\,g^{-1}$ SSA and 10.4 nm average pore diameter [APD]) was rather similar to that for SnO_2-T/PANi ($189.1\,m^2\,g^{-1}$ SSA and 12.7 nm APD) as against that for SnO_2-S/PANi ($111.6\,m^2\,g^{-1}$ SSA and 6.3 nm APD), suggesting that T serves as the backbone for architecture formation.

From the low-magnification transmission electron microscopy (TEM; Tecnai G^2 F20 S-TWIN, FEI, USA) image (Fig. 3A), SnO_2 NPs (4.4 ± 1.2 nm) formed agglomerates via the Brownian motion under the air flow, and blurry spots (i.e., SnO_2 NPs) in the agglomerate corresponded to the PANi overlayers, demonstrating that SnO_2 NPs are encapsulated by PANi layers as vesicles during the UV stiffening and drying of the SnO_2/PANi droplets. The high-magnification TEM image revealed a lattice fringe of 0.33 nm, corresponding to the (1 1 0) plane of tetragonal SnO_2 [34]. With the incorporation of TS, the morphology of SnO_2/PANi converted into three-dimensional bunches, revealing the intervention of SnO_2 into TS matrices (i.e., SnO_2 dots were hardly

visible in the bunch structures.) (Fig. 3B). The redistribution of SnO_2 NPs was possibly related to the shattering of SnO_2 agglomerates into ultrafine (< 10 nm) particles near the spray nozzle because of the sudden pressure change (i.e., reduction of the cohesive strength between ultrafine SnO_2 particles in an agglomerate) [35]. The shattered SnO_2 particles were subsequently dispersed among the TS matrices to form SnO_2-TS before re-agglomeration, and SnO_2-TS was successively encapsulated by the PANi layers to form SnO_2-TS/PANi during stiffening and drying. The high-magnification TEM image revealed two lattice fringes, i.e., 0.33 nm (tetragonal SnO_2) and 0.34 nm (graphitic carbon), respectively, supporting the redistribution of SnO_2 into the TS matrices. This SnO_2 redistribution with ultrafine scales suggested that the single-pass flow assembly is versatile for assembling various desired architectures (i.e., ultrafine TMO particles dispersed among conductive networks) for high performance lithium storage. Elemental mapping analyses using energy-dispersive X-ray spectroscopy (EDX; JED-2300, JEOL, Japan) further supported the incorporation of SnO_2 (Sn map), TS (C map), and PANi (N map) during the assembly to form SnO_2-TS/PANi (Fig. 3C).

Fig. 4 shows the electrochemical performance of the assembled SnO_2-TS/PANi composites as lithium anodes. Cyclic voltammetry (CV) curves of the anode for the first five cycles exhibited two shoulder peaks at ~0.93 and 0.42 V, respectively, in the first cathodic cycle, corresponding to the formation of a solid electrolyte interphase (SEI) with the reduction of SnO_2 to Sn and of Li_xSn with Li_xC (Fig. 4A) [36]. For the first anodic cycle, two broad bands were observed at ~1.3 and 0.5 V, corresponding to the lithium extracted from Li_xSn and Li_xC, respectively. The CV curves did not significantly change in the subsequent four cycles (2nd–5th cycles), implying that the assembled anode is suitable for securing cycle stability. From the first charge–discharge curves at a current density of $0.1\,A\,g^{-1}$ (Fig. 4B), a Coulombic efficiency of 71.6% was observed, and the capacity loss was mainly related to the formation of SEI films on SnO_2-TS/PANi anodes with Li_2O formation and electrolyte degradation [36]. In the subsequent cycles (2nd–50th cycles), differences in the charge–discharge capacity were remarkably reduced; thus, the Coulombic efficiency increases to > 97%. Fig. 4C shows the galvanostatic cycling performance of the SnO_2-TS/PANi anodes at a current density of $0.1\,A\,g^{-1}$, as well as SnO_2/PANi and TS/PANi for comparison. From the 20th cycle, the decreased specific capacity of SnO_2-TS/PANi gradually increased,
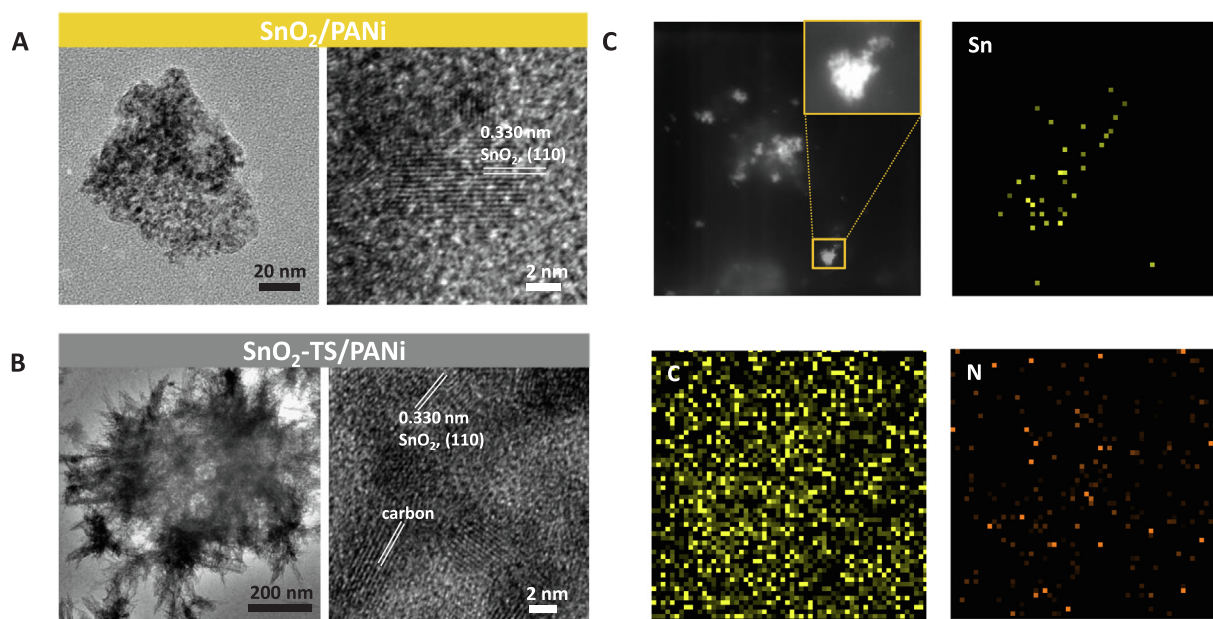

Fig. 3. Morphological and elemental analyses of the assembled SnO_2/PANi and SnO_2-TS/PANi composites. (A, B) Low- and high-magnification TEM images of the composites. (C) EDX maps of SnO_2-TS/PANi to confirm the coexistence of SnO_2 (tin, Sn), TS (carbon, C), and PANi (nitrogen, N).
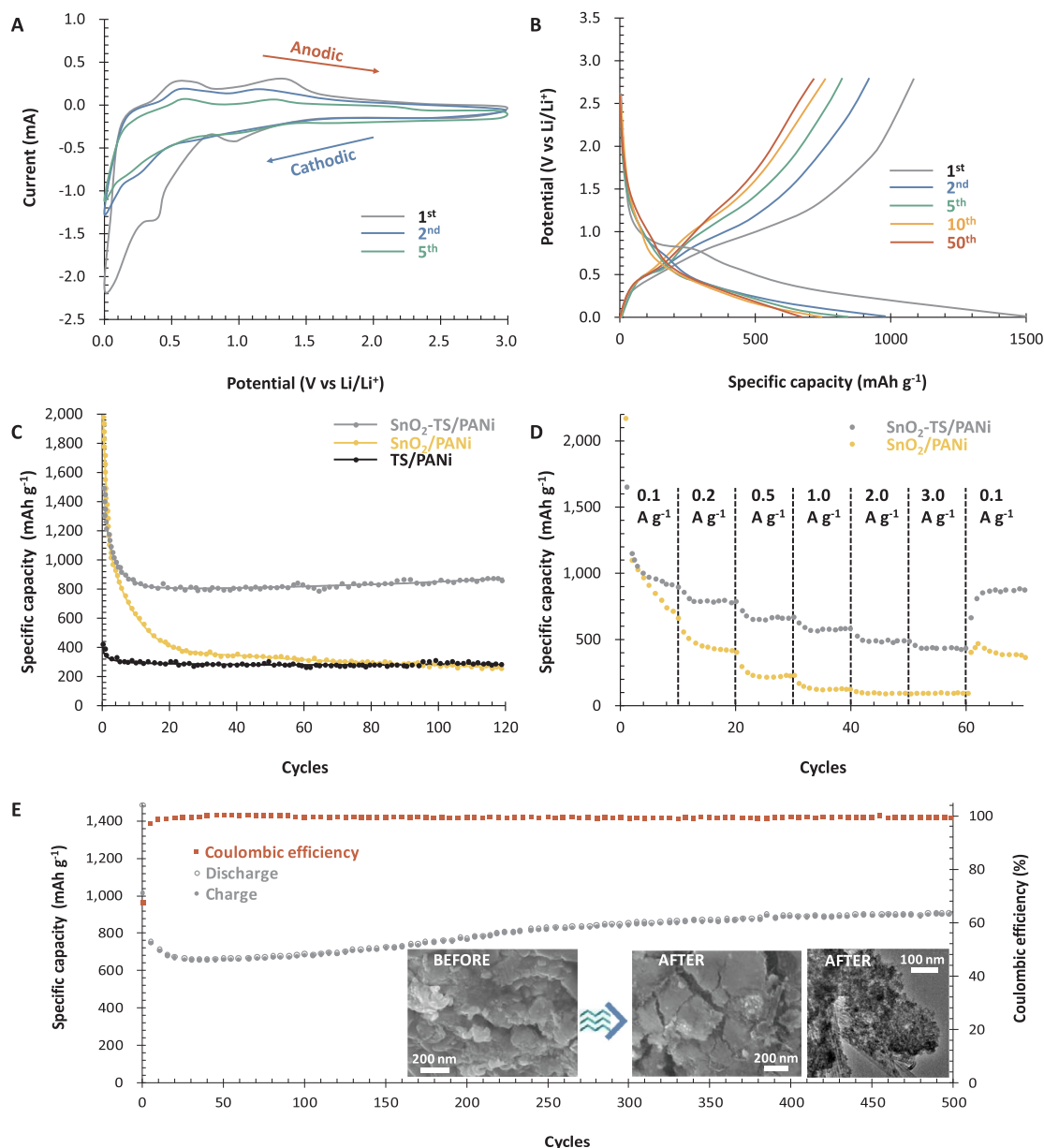
Fig. 4. Electrochemical analyses of the assembled SnO_2/PANi and SnO_2-TS/PANi composites. (A, B) CV and charge–discharge (at a current density of $0.1\,A\,g^{-1}$) curves of the SnO_2-TS/PANi composite. (C) Cyclabilities of the composite, including SnO_2/PANi and TS/PANi for comparison, at a current density of $0.1\,A\,g^{-1}$. (D) Rate capabilities of the composite at various current densities (0.1–$3.0\,A\,g^{-1}$), including SnO_2/PANi. (E) Cyclabilities and Coulombic efficiencies of the composite at a current density of $0.5\,A\,g^{-1}$. Inset SEM images of the composite anodes before and after 500 cycles at a current density of $0.5\,A\,g^{-1}$. Inset TEM image exhibits the anode after 500 cycles at the same current density.

reaching $840\,mAh\,g^{-1}$ after 100 cycles, possibly related to the thermal formation of Sn–N bonds between SnO_2 and TS surfaces because of the intervention of PANi, leading to the strong attachment of SnO_2 particles on the TS surfaces to prevent the aggregation of SnO_2 [37]. The reconstruction of stacked SnO_2-TS/PANi via thermal curing during cycling might also be related to the stable cyclability because of the improved contact between SnO_2-TS/PANi and the electrolyte [28]. In addition, analogous phenomena were observed for the SnO_2-T/PANi and SnO_2-S/PANi anodes (Fig. S4) although cyclabilities depended on their architectures. On the other hand, the specific capacity of SnO_2/PANi reduced more significantly during cycling, reaching $230\,mAh\,g^{-1}$ after 100 cycles although PANi was layered on the SnO_2 NP surface. This result highlighted the importance of the incorporation of TS to provide not only a support for the redistribution of SnO_2 agglomerates during the assembly but also shield the aggregation suppression of SnO_2

NPs during cycling. By the consideration of the results observed for TS/PANi, the suitable dispersion of SnO_2 NPs on the matrices can be a critical parameter for the anode assembly to synergize the effects of active components (i.e., SnO_2, TS, and PANi) for achieving cycle stabilities. The rate capabilities of SnO_2-TS/PANi were inversely proportional to the current density (0.1–$3.0\,A\,g^{-1}$) (Fig. 4D). SnO_2-TS/PANi exhibited capabilities significantly greater than those of SnO_2/PANi, similar to the cyclability measurement; in addition, SnO_2-TS/PANi was tolerable to recover the capability when the current density was replaced by the initial value ($0.1\,A\,g^{-1}$). For electrochemical impedance spectroscopy (EIS) measurement (Fig. S5), SnO_2-TS/PANi ($87.6\,\Omega$) exhibited a significantly lower charge transfer resistance compared with SnO_2/PANi ($163.2\,\Omega$), further proving better electrochemical kinetics in the anode. The cycle stability of the SnO_2-TS/PANi anode was further validated for 500 cycles at a current density of $0.5\,A\,g^{-1}$ (Fig. 4E), and
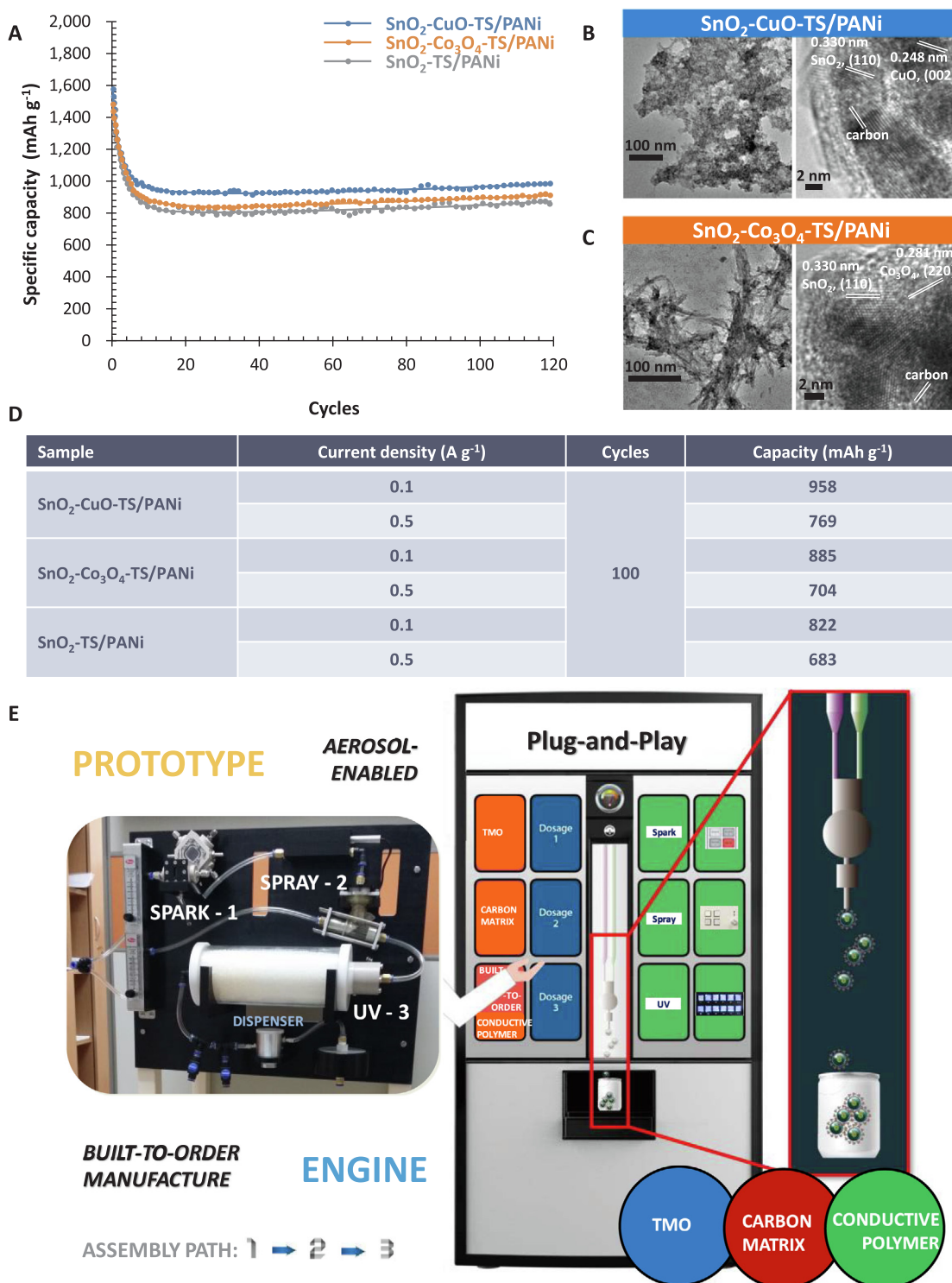
Fig. 5. Cyclability and morphology of other composites assembled using a prototype of the plug-and-play assembly platform. (A) Cyclabilities of SnO$_2$−CuO-TS/PANi and SnO$_2$−Co$_3$O$_4$-TS/PANi composite anodes at a current density of 0.1 A g^{-1}, including SnO$_2$-TS/PANi for comparison. (B, C) Low- and high-magnification TEM images of the SnO$_2$−CuO-TS/PANi and SnO$_2$−Co$_3$O$_4$-TS/PANi composites. (D) Electrochemical properties of the SnO$_2$−CuO-TS/PANi and SnO$_2$−Co$_3$O$_4$-TS/PANi composite anodes, including SnO$_2$-TS/PANi for comparison. (E) Digital image of a prototype engine for the plug-and-play assembly and schematic of the engine integrated system for the built-to-order manufacture of various composite anodes.

the resulting capacity was constant at ~840 mAh g^{-1} with a Columbic efficiency of ~100% after 500 cycles. The anode exhibited capacity decay before the 20th cycle probably due to the formation of stable SEI films [38]. The subsequent gradual increase in capacity might be attributed to the delay contact between the composite and electrolyte [39]. This result further supported the suitability of the assembled anode architecture for the introduction of superior charge transport and electrochemical activity for achieving cyclic stability. The inset of scanning electron microscopy (SEM; JSM-6500F, JEOL, Japan) images revealed microscopic morphologies of the anodes before and after cycling (500 cycles). Another inset image shows a representative TEM image of the anode after the cycling. The structure did not significantly

disintegrate, revealing that the SnO$_2$-TS/PANi architecture is suitable to accommodate the volume expansion of SnO$_2$ NPs during cycling. In addition, comparison in discharge capacity of half- and full-cell setup was carried out (Fig. S6). The half-cell (with lithium metal foil) exhibited a drastic drop of the capacity after 640 cycles, which might be due to the formation of lithium dendrites (causing a short circuit), whereas, the full-cell showed a slow linear decay in the capacity even after 1000 cycles. The smaller content of lithium in the full-cell setup might avoid the formation of lithium dendrites in cycling, suggesting that combination of different cell configurations might be useful to modulate cycling stability.

Modulating cyclabilities were achieved by employing different spark ablation configurations (i.e., Sn—Cu and Sn—Co) instead of the Sn–Sn configuration under air flow because the combination of other TMOs (i.e., based on Cu-, Fe-, and Co-) with SnO$_2$ enhanced electrochemical performance [40,41]. Then, SnO$_2$—CuO- or SnO—Co$_3$O$_4$-laden flow was identically connected to the mechanical spray (for TS/PANi incorporation) and UV exposure (for stiffening and drying) devices to assemble a SnO$_2$—CuO-TS/PANi or SnO—Co$_3$O$_4$-PANi anode. Fig. S7 shows the morphologies of SnO$_2$-, SnO$_2$—CuO-, and SnO—Co$_3$O$_4$-TS/PANi composites. There are no notable differences in morphology, which imply that the plug-and-play platform can manufacture similar anode architectures even modulating TMO composition. Fig. 5A shows the cyclabilities of the SnO$_2$—CuO-TS/PANi and SnO—Co$_3$O$_4$-TS/PANi anodes at a current density of 0.1 A g^{-1} (for 120 cycles): Enhanced stabilities compared to SnO$_2$-TS/PANi were observed. Such enhanced cyclability was possibly related to the catalytic activity of co-dispersed CuO or Co$_3$O$_4$ particles on the TS matrices (confirmed by TEM measurements; Fig. 5B and C) to accelerate the Li$_2$O decomposition and Sn oxidation during discharge [40], verifying that the proposed assembly is suitable to demonstrate the reconfiguration capability with modulating electrochemical performance (Fig. 5D). According to TEM analyses, in addition, the analogous redistribution of SnO$_2$—CuO and SnO—Co$_3$O$_4$ agglomerates on the matrices confirmed the serial connection of spark ablation, mechanical spraying, and UV exposure for realizing the reconfigurable plug-and-play platform for built-to-order anode manufacture. Fig. 5E shows an aerosol-enabled prototype comprising the spark, spray, and UV units for the single-pass assembly of composite anodes under air flow. The integration of this platform as an engine in a vending-machine-like system can be expected to facilitate the continuous built-to-order manufacture of the composite anodes. The combination of a plug-and-play platform as the dispenser and a roll-to-roll fabrication system [8] can also be a stepping stone to timely provide commercial opportunities for newly developed active materials to various energy-storage devices.

3. Conclusions

Unlike previously reported studies on lithium storage that focused on new materials and architectures, in this study, a plug-and-play assembly platform was introduced to achieve the built-to-order manufacture of composite anodes with modulating electrochemical performance for providing realizable opportunities to lithium-based batteries. Different architectures of composite anodes under an ambient single-pass air flow were conveniently achieved by connecting atmospheric spark ablation, mechanical spraying, and UV exposure devices in series. The lithium storage performance was modulated by the combination of different TMO NPs (SnO$_2$, SnO$_2$—CuO, and SnO$_2$—Co$_3$O$_4$) and carbon matrices (TS, T, and S) with PANi to form composite slurry droplets. These droplets were dynamically stiffened and dried by passage through a 254-nm UV and silica-gel-installed hollow tube still under an air flow; thus, the composites are continuously dispensed for the fabrication of anodes via simply switching the plug-and-play devices on. In less than 15 s, the assembly achieved comparable capacities, rate capabilities, and cycling stabilities via compensation of the volume change of TMO NPs and improvement in charge transport via the formation of

conductive matrices. The built-to-order manufacture of various composite anodes corresponding to the plug-and-play operation may not only provide realizable opportunities for customized lithium-based batteries but also offer conceptual insights into the digitization of electrode fabrication for energy-storage devices.

Acknowledgements

Appendix A. Supplementary data

Supplementary data to this article can be found online at https://doi.org/10.1016/j.cej.2019.02.006.

References

[1] P. Zheng, Z. Dai, Y. Zhang, K.N. Dinh, Y. Zheng, H. Fan, J. Yang, R. Dangol, B. Li, Y. Zong, Q. Yan, X. Liu, Scalable synthesis of SnS$_2$/S-doped graphene composites for superior Li/Na-ion batteries, Nanoscale 9 (2017) 14820–14825.
[2] H. Zhao, H. Zeng, Y. Wu, S. Zhang, B. Li, Y. Huang, Facile scalable synthesis and superior lithium storage performance of ball-milled MoS$_2$-graphite nanocomposites, J. Mater. Chem. A 3 (2015) 10466–10470.
[3] B. Huang, Z. Pan, X. Su, L. An, Tin-based materials as versatile anodes for alkali (earth)-ion batteries, J. Power Sources 395 (2018) 41–59.
[4] Z. Xing, Z. Wang, A. Yu, Z. Chen, Aqueous intercalation-type electrode materials for grid-level energy storage: beyond the limits of lithium and sodium, Nano Today 50 (2018) 229–244.
[5] H. Hao, Z. Mu, X. Jiang, Z. Liu, F. Zhao, GHG emissions from the production of lithium-ion batteries for electric vehicles in China, Sustainability 9 (2017) 504.
[6] L. Lee, B. Kang, S. Han, H.–E. Kim, M.D. Lee, J.H. Bang, A generalizable top-down nanostructuring method of bulk oxides: sequential oxygen–nitrogen exchange reaction, Small 14 (2018) 1801124.
[7] J. Schnell, T. Günther, T. Knoche, C. Vieider, L. Köhler, A. Just, M. Keller, S. Passerini, G. Reinhart, All-solid-state lithium-ion and lithium-metal batteries – paving the way to large-scale production, J. Power Sources 382 (2018) 160–175.
[8] M. Bai, K. Xie, K. Yuan, K. Zhang, N. Li, C. Shen, Y. Lai, R. Vajtai, P. Ajayan, B. Wei, A scalable approach to dendrite-free lithium anodes via spontaneous reduction of spray-coated graphene oxide layers, Adv. Mater. 30 (2018) 1801213.
[9] S.H. Choi, J.-H. Lee, Y.C. Kang, Perforated metal oxide–carbon nanotube composite microspheres with enhanced lithium-ion storage properties, ACS Nano 9 (2015) 10173–10185.
[10] L. Zhang, X. Liu, Y. Dou, B. Zhang, H. Yang, S. Dou, H. Liu, Y. Huang, X. Hu, Mass production and pore size control of holey carbon microcages, Angew. Chem. Int. Ed. 56 (2017) 13790–13794.
[11] J.H. Byeon, Y.-W. Kim, Tin–tin dioxide@hollow carbon nanospheres synthesized by aerosol catalytic chemical vapor deposition for high-density lithium storage, ChemCatChem 6 (2014) 1567–1569.
[12] F. Meierhofer, H. Li, M. Gockeln, R. Kun, T. Grieb, A. Rosenauer, U. Fritsching, J. Kiefer, J. Birkenstock, L. Mädler, S. Pokhrel, Screening precursor–solvent combinations for Li$_4$Ti$_5$O$_{12}$ energy storage material using flame spray pyrolysis, ACS Appl. Mater. Interfaces 9 (2017) 37760–37777.
[13] A. Jahel, C.M. Ghimbeu, L. Monconduit, C. Vix-Guterl, Confined ultrasmall SnO$_2$ particles in micro/mesoporous carbon as an extremely long cycle-life anode material for lithium-ion batteries, Adv. Energy Mater. 4 (2014) 1400025.
[14] Z. Zhang, L. Wang, J. Xiao, F. Xiao, S. Wang, One-pot synthesis of three-dimensional graphene/carbon nanotube/SnO$_2$ hybrid architectures with enhanced lithium storage properties, ACS Appl. Mater. Interfaces 7 (2015) 17963–17968.
[15] S.K. Park, H.-K. Kim, K.C. Roh, K.–B. Kim, H.S. Park, The confinement of SnO$_2$ nanocrystals into 3D RGO architectures for improved rate and cyclic performance of LIB anode, CrystEngComm 18 (2016) 6049–6054.
[16] H. Yang, N. Wang, Q. Xu, Z. Chen, Y. Ren, J.M. Razal, J. Chen, Fabrication of graphene foam supported carbon nanotube/polyaniline hybrids for high-performance supercapacitor applications, 2D Mater. 1 (2014) 034002.
[17] Z. Xiao, J. Meng, Q. Li, X. Zhang, Z. Liu, B. Wen, C. Han, L. Mai, General and precise carbon confinement of functional nanostructures derived from assembled metal-–phenolic networks for enhanced lithium storage, J. Mater. Chem. A 6 (2018) 18605–18614.
[18] C. Han, B. Zhang, K. Zhao, J. Meng, Q. He, P. He, W. Yang, Q. Li, L. Mai, Oxalate-assisted formation of uniform carbon-confined SnO$_2$ nanotubes with enhanced lithium storage, Chem. Commun. 53 (2017) 9542–9545.
[19] J. Lefebvre, J. Ding, Z. Li, P. Finnie, G. Lopinski, R.L. Malenfant, High-purity semiconducting single-walled carbon nanotubes: a key enabling material in emerging electronics, Acc. Chem. Res. 50 (2017) 2479–2486.
[20] K. Moothi, G.S. Simate, R. Falcon, S.E. Iyuke, M. Meyyappan, Carbon nanotube synthesis using coal pyrolysis, Langmuir 31 (2015) 9464–9472.
[21] K.R. Paton, E. Varrla, C. Backes, R.J. Smith, U. Khan, A. O'Neill, C. Boland, M. Lotya, O.M. Istrate, P. King, T. Higgins, S. Barwich, P. May, P. Puczkarski,

I. Ahmed, M. Moebius, H. Pettersson, E. Long, J. Coelho, S.E. O'Brien, E.K. McGuire, B.M. Sanchez, G.S. Duesberg, N. McEvoy, T.J. Pennycook, C. Downing, A. Crossley, V. Nicolosi, J.N. Coleman, Scalable production of large quantities of defect-free few-layer graphene by shear exfoliation in liquids, Nat. Mater. 13 (2014) 624–630.

[22] C. Shan, H. Tang, T. Wong, L. He, S.-T. Lee, Facile synthesis of a large quantity of graphene by chemical vapor deposition: an advanced catalyst carrier, Adv. Mater. 24 (2012) 2491–2495.

[23] J. Yan, T. Wei, B. Shao, Z. Fan, W. Qian, M. Zhang, F. Wei, Preparation of a graphene nanosheet/polyaniline composite with high specific capacitance, Carbon 48 (2010) 487–493.

[24] J. Shen, C. Yang, X. Li, G. Wang, High-performance asymmetric supercapacitor based on nanoarchitectured polyaniline/graphene/carbon nanotube and activated graphene electrodes, ACS Appl. Mater. Interfaces 5 (2013) 8467–8476.

[25] Q. Wu, Y. Xu, Z. Yao, A. Liu, G. Shi, Supercapacitors based on flexible graphene/polyaniline nanofiber composite films, ACS Nano 4 (2010) 1963–1970.

[26] V. Etacheri, G.A. Seisenbaeva, J. Caruthers, G. Daniel, J.-M. Nedelec, V.G. Kessler, V.G. Pol, Ordered network of interconnected SnO_2 nanoparticles for excellent lithium-ion storage, Adv. Energy Mater. 5 (2015) 1401289.

[27] B. Zhang, Q.B. Zheng, Z.D. Huang, S.W. Oh, J.K. Kim, SnO_2–graphene–carbon nanotube mixture for anode material with improved rate capacities, Carbon 49 (2011) 4524–4534.

[28] D. Zhou, W.-L. Song, L.–Z. Fan, Hollow core–shell SnO_2/C fibers as highly stable anodes for lithium-ion batteries, ACS Appl. Mater. Interfaces 7 (2015) 21472–21478.

[29] B. Huang, J. Yang, Y. Zou, L. Ma, X. Zhou, Sonochemical synthesis of SnO_2/carbon nanotubes encapsulated in graphene sheets composites for lithium ion batteries with superior electrochemical performance, Electrochim. Acta 143 (2014) 63–69.

[30] J. Porwal, N. Karanwal, S. Kaul, S.L. Jain, Carbocatalysis: N-doped reduced graphene oxide catalyzed esterification of fatty acids with long chain alcohols, New J. Chem. 40 (2016) 1547–1553.

[31] T. Peng, H. Sun, T. Peng, B. Liu, X. Zhao, Structural regulation and electroconductivity change of nitrogen-doping reduced graphene oxide prepared using p-phenylene diamine as modifier, Nanomaterials 7 (2017) 292.

[32] J.H. Byeon, J. Hwang, Morphology of metallic nanoparticles as a function of deposition time in electroless deposition of metal on multi-walled carbon nanotubes, Surf. Coat. Technol. 203 (2008) 357–363.

[33] Y. Zou, X. Zhou, J. Xie, Q. Liao, B. Huang, J. Yang, A corn-like graphen–SnO_2–carbon nanofiber composite as a high-performance Li-storage material, J. Mater. Chem. A 2 (2014) 4524–4527.

[34] J. Lin, Z. Peng, C. Xiang, G. Ruan, Z. Yan, D. Natelson, J.M. Tour, Graphene nanoribbon and nanostructured SnO_2 composite anodes for lithium ion batteries, ACS Nano 7 (2013) 6001–6006.

[35] J.H. Byeon, J.T. Roberts, Aerosol based fabrication of thiol-capped gold nanoparticles and their application for gene transfection, Chem. Mater. 24 (2012) 3544–3549.

[36] C. Ma, W. Zhang, Y.-S. He, Q. Gong, H. Che, Z.–F. Ma, Carbon coated SnO_2 nanoparticles anchored on CNT as a superior anode material for lithium-ion batteries, Nanoscale 8 (2016) 4121–4126.

[37] X. Zhou, L.-J. Wan, Y.–G. Guo, Binding SnO_2 nanocrystals in nitrogen-doped graphene sheets as anode materials for lithium-ion batteries, Adv. Mater. 25 (2013) 2152–2157.

[38] X. Zhou, Z. Dai, S. Liu, J. Bao, Y.-G. Guo, Ultra-uniform SnO_x/carbon nanohybrids toward advanced lithium-ion battery anodes, Adv. Mater. 26 (2014) 3943–3949.

[39] H. Wu, G. Yu, L. Pan, N. Liu, M.T. McDowell, Z. Bao, Y. Cui, Stable Li-ion battery anodes by in-situ polymerization of conducting hydrogel to conformally coat silicon nanoparticles, Nat. Commun. 4 (2013) 1943.

[40] Y. Wang, Z.X. Huang, Y. Shi, J.I. Wong, M. Ding, H.Y. Yang, Designed hybrid nanostructure with catalytic effect: beyond the theoretical capacity of SnO_2 anode material for lithium ion batteries, Sci. Rep. 5 (2015) 9164.

[41] D. Li, D. Yan, X. Zhang, J. Li, T. Lu, L. Pan, Porous CuO/reduced graphene oxide composites synthesized from metal–organic frameworks as anodes for high-performance sodium-ion batteries, J. Colloid Interface Sci. 497 (2017) 350–358.